Supplementary Information for:

Critical charge fluctuations and emergent coherence in a strongly correlated excitonic insulator

Pavel A. Volkov,[1*] Mai Ye,[1*] Himanshu Lohani,[2] Irena Feldman,[2]
Amit Kanigel,[2] Girsh Blumberg[1,3*]

[1]Department of Physics and Astronomy, Rutgers University, Piscataway, NJ 08854, USA
[2]Department of Physics, Technion - Israel Institute of Technology, Haifa 32000, Israel
[3]National Institute of Chemical Physics and Biophysics, 12618 Tallinn, Estonia

[*]Corresponding author: girsh@physics.rutgers.edu (G.B.)

Contents

Supplementary Note 1 Experimental details

Supplementary Note 1.1 Resistance Measurement

Fig 1(a) shows the resistance as a function of the temperature. We find a small break in the resistivity at the transition temperature $T_c \simeq 327$ K, shown in the inset. This small change appears more prominent in Fig 1(b), where the activation energy (- k_B T^2 $\frac{\partial \ln(R(T))}{\partial T}$) is presented. This result is consistent with the previous report [1] within the accuracy of the measurement.

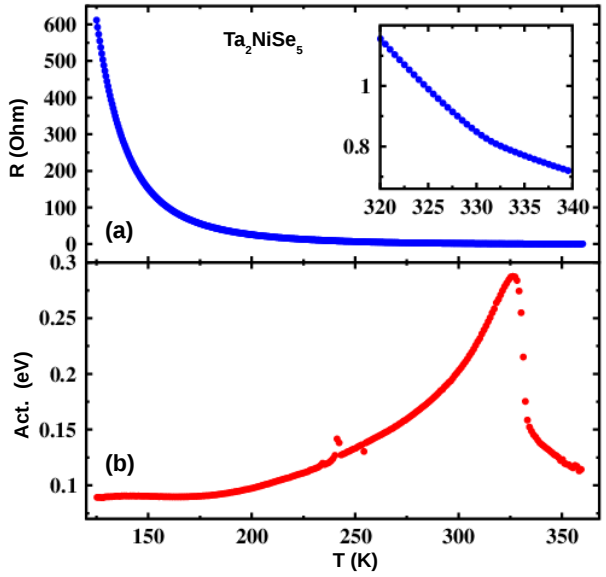

Supplementary Figure 1: Resistance (a) and activation energy (b) plot of Ta_2NiSe_5. Inset of (a) shows a small break in the resistance around the transition temperature 327 K.

Supplementary Note 1.2 Heating rate estimation using Stokes/Anti-Stokes analysis

In thermal equilibrium, the Stokes (absorption) scattering cross section $I_{\rm S}$ and Anti-Stokes (emission) cross section $I_{\rm AS}$ are related by the detailed balance principle [2]

$$nI_{\rm S}(\omega) = (n+1)I_{\rm AS}(\omega)\,, \tag{1}$$

in which n stands for the Bose factor

$$n(\omega, T) = \frac{1}{\exp(\hbar\omega/k_{\rm B}T) - 1}\,, \tag{2}$$

where $\hbar$ is the reduced Planck's constant, ω is frequency, $k_{\rm B}$ is the Boltzmann's constant, and T is the temperature in the laser spot. Using Eq. (1-2), the temperature can be obtained as

$$T = \frac{\hbar\omega}{k_{\rm B}\log(I_{\rm S}(\omega)/I_{\rm AS}(\omega)} \ . \tag{3}$$

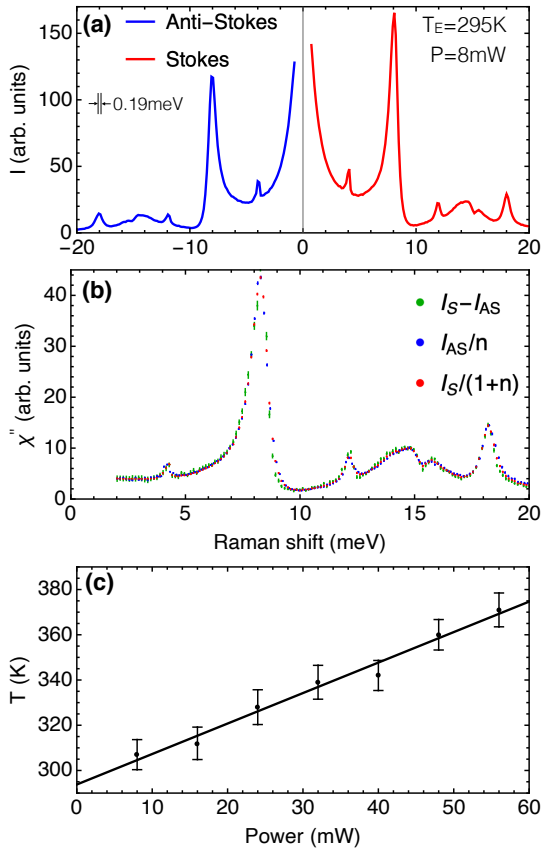

Supplementary Figure 2: Stokes-Anti-Stokes analysis of the spectra taken in ac polarization geometry [3]: (a) Measured Raman cross-section $I(\omega)$ that includes both the Stokes (red line, $\omega > 0$) and Anti-Stokes (blue line, $\omega < 0$) parts measured at environmental temperature $T_{\rm E} = 295$ K with laser power P = 8 mW. (b) The Raman response $\chi''(\omega)$ calculated from the measured spectra in (a) [see Eq. 4]. The laser-spot temperature, which appears in the Bose factor n, is 307 K. The response obtained using three equivalent ways in Eq. 4 agree well, showing that the detailed balance relation Eq. (1) holds. The spectral resolution is 0.19 meV for panels (a-b). (c) The laser-power dependence of the laser-spot temperature (Eq. 3). The straight line represents a linear fit corresponding to heating rate of 1.29 ± 0.17 K mW^{-1}.

The Raman susceptibility can then be obtained in three equivalent ways (using Eq. 1):

$$\chi''(\omega) = \frac{I_{\rm S}(\omega)}{n(\omega)+1} = \frac{I_{\rm AS}(\omega)}{n(\omega)} = I_{\rm S}(\omega) - I_{\rm AS}(\omega) \tag{4}$$

We studied the Stokes and Anti-Stokes cross section relation for the ac scattering geometry at 295 K environmental temperature with varying laser power. In Fig. 2 we show the results measured with 8 mW laser power as an example. The Raman responses calculated from Stokes and Anti-Stokes cross sections match well with the temperature at the laser spot being 307 K. We use Eq. (3) with the phonon intensity integrated from 7.5 to 8.5 meV to calculate the temperature at the laser spot. By a linear fit to the power dependence of the laser-spot temperature, we find the heating rate to be $1.29\pm0.17\,\mathrm{K\,mW^{-1}}$.

Supplementary Note 1.3 Fitting model for the Raman susceptibility

Supplementary Note 1.3.1 Temperatures above T_c

Here we describe the procedure we used to fit the ac Raman susceptibility around T_c characterized by strongly asymmetric features, see Fig. 2d and Fig. 3 of the main text. In particular, it is well known that such asymmetry cannot be captured by a conventional Lorentzian oscillator lineshape and instead signifies an interference effect arising from interaction between a sharp mode and an excitation continuum [4; 5]. The general result following from Fermi's Golden Rule [5] is

$$I(\omega) = \mathrm{Im} \sum_{i,j=\mathrm{e,p}} \{t_i \langle i|G(\omega+i\delta)|j\rangle t_j\}\,,\; G(z) = \begin{bmatrix} G_\mathrm{p}^{-1}(z) & v \\ v & G_\mathrm{e}^{-1}(z) \end{bmatrix}^{-1}, \tag{5}$$

where $t_{\mathrm{e/p}}$ are the Raman excitation matrix elements and $G_{\mathrm{e/p}i}(\omega)$ are the Green's functions of the electronic continuum and of the phonon mode (such that the corresponding susceptibilities of the individual components are given by $t^2_{\mathrm{e/p}i}G_{\mathrm{e/p}i}(\omega)$) and v is the interaction matrix element between them (which is approximated by a frequency-independent constant). In the simplest case, for an infinite continuum with a constant density of states ρ (such that $G_\mathrm{e}(\omega+i\delta) = i\pi\rho$) and a delta-function-like sharp mode $G_\mathrm{p}^{-1}(\omega+i\delta) = \omega_\mathrm{p} - \omega$ one gets [6; 7]:

$$I(\omega) = \frac{t_\mathrm{e}^2\pi\rho(\omega_\mathrm{p} - \omega - vt_\mathrm{p}/t_\mathrm{e})^2}{(\omega_\mathrm{p}-\omega)^2 + (v^2\pi\rho)^2}, \tag{6}$$

where it is evident that the parameter $vt_\mathrm{p}/t_\mathrm{e}$ controls the asymmetry of the peak lineshape. Note that the total intensity can be smaller than the continuum intensity: e.g. at $\omega = \omega_\mathrm{p} - vt_\mathrm{p}/t_\mathrm{e}$ the total intensity vanishes ("Fano antiresonance"), while the continuum intensity at this frequency is equal to $t_\mathrm{e}^2\pi\rho$. This effect highlights the role of interference in the Fano model and a similar effect is observed in our data (Fig. 3c of the main text, around 10 meV).

To describe the results obtained we need to adjust this simple model in the following ways. First, in our results we have observed three distinct phonon peaks. Taking into account their rather close spacing we need to generalize the above to include three sharp independent modes and take the interaction between continuum and each of the modes into account.

For the bare phonon Green's function, we use

$$G_{\mathrm{p}i}(\omega) = -\left(\frac{1}{\omega - \omega_{\mathrm{p}i} + i\gamma_{\mathrm{p}i}} - \frac{1}{\omega + \omega_{\mathrm{p}i} + i\gamma_{\mathrm{p}i}}\right) , \tag{7}$$

such that $\mathrm{Im}\chi_{\mathrm{p}i}(\omega)$ is an odd function of ω (the requirement $\chi''(-\omega) = -\chi''(\omega)$ arises due to the requirement of the real-time response to be real). The parameters $\omega_{\mathrm{p}i}$ and $\gamma_{\mathrm{p}i}$ respectively have the physical meaning of the mode energy and the half width at half maximum (HWHM).

Finally, the electronic continuum contribution has been found to be best described by a purely relaxational response $\chi^{-1}_{\mathrm{cont}}(\omega) \propto -i\Gamma\omega + \omega_0^2$ that correspond to the overdamped ($\Gamma \gg \omega_0$) limit of the Drude-Lorentz model. This form follows from the time-dependent Ginzburg-Landau [8] description of the dynamics of the electronic order parameter φ, which can be applied to a diverse range of systems from charge-density wave [9; 10] to superconducting [11] ones. In our case, due to absence of a gap above T_{c}, the dynamics of the order parameter can be expected to be of relaxational type, resulting in the following time-dependent Ginzburg-Landau equation for the electronic order parameter φ:

$$\begin{aligned} -\Gamma\partial_t\varphi &= \frac{dF}{d\varphi}, \\ F[\varphi, T] &= a(T)\frac{\varphi^2}{2} + b\frac{\varphi^4}{4}, \end{aligned} \tag{8}$$

where $a(T) > 0$ for $T > T_{\mathrm{c}}^{\mathrm{el}}$ and $a(T_{\mathrm{c}}^{\mathrm{el}}) = 0$. Above T_{c} the quartic term in $F[\varphi, T]$ can be neglected resulting in $-\Gamma\partial_t\varphi = a(T)\varphi$. For an external source (which is the quadrupolar field of xz symmetry provided by the photons in the Raman process), the response function becomes:

$$\chi_{\mathrm{el}}(\omega, T) = \frac{C}{i\Gamma\omega + a(T)} = \frac{C/\Gamma}{i\omega + a(T)/\Gamma},$$

which is determined by two parameters: C/Γ and $a(T)/\Gamma$. As the above form resembles an overdamped oscillator, we have used the notation $a(T) \equiv \omega_0^2(T)$ for illustrative purposes. Furthermore, for the case of a conventional exciton, the response is expected to be that of a usual oscillator, similar to phononic modes; we found this notation useful to explain the physics of this mode. Thus, we have used the following form of the continuum response:

$$G_{\mathrm{e}}^{-1}(\omega) = -i\omega + \Omega_{\mathrm{e}}, \tag{9}$$

where $\Omega_{\mathrm{e}} = \frac{\omega_0^2}{\Gamma}$.

Summarizing the above, we use the following model to fit the data:

$$\chi''(\omega) = \mathrm{Im}\sum_{ij} T_i G_{ij}(\omega) T_j \ , \tag{10}$$

where $T = \begin{pmatrix} t_{p1} & t_{p2} & t_{p3} & t_e \end{pmatrix}$ is the matrix element of the Raman light scattering process, and G is defined by

$$G = (G_0^{-1} - V)^{-1}. \tag{11}$$

where

$$G_0 = \begin{pmatrix} G_{p1} & 0 & 0 & 0 \\ 0 & G_{p2} & 0 & 0 \\ 0 & 0 & G_{p3} & 0 \\ 0 & 0 & 0 & G_e \end{pmatrix}, \tag{12}$$

$$V = \begin{pmatrix} 0 & 0 & 0 & v_1 \\ 0 & 0 & 0 & v_2 \\ 0 & 0 & 0 & v_3 \\ v_1 & v_2 & v_3 & 0 \end{pmatrix}. \tag{13}$$

This model can be thought of as a generalization of (5) for three phonons, where $G_{\mathrm{p}i}^{-1}$ (i=1,2,3) correspond to the $\mathrm{B}_{2g}^{(i)}$ phonon mode and have the form (7), and the parameter v_i describe the coupling strength of this mode to the electronic excitations which are represented by G_e^{-1} that has the form (9).

In Fig. 3 (red lines) we present the obtained fits using Eq. (11-13) (for parameters see Sec. 1.3.3) for temperatures above T_{c} in linear scale (as opposed to logarithmic used in Fig. 3 of the main text). Furthermore, we define the bare excitonic (blue line) and phononic (green line) responses as:

$$\chi''_{\mathrm{opt}}(\omega) = \sum_{i=1}^{3} t_{\mathrm{p}i}^2 \mathrm{Im}G_{\mathrm{p}i}(\omega);\ \chi''_{\mathrm{cont}}(\omega) = \frac{t_{\mathrm{e}}^2 \omega}{\omega^2 + \Omega_{\mathrm{e}}^2}. \tag{14}$$

One observes that the fit quality away from T_{c} is excellent, but becomes slightly worse on approaching T_{c}. This can be related to the presence of nonlinear exciton-phonon interactions that are not included in the Fano model and may become important close to the transition (see also discussion on top of page 7 of the main text).

Supplementary Note 1.3.2 Temperatures below T_{c}

At $T < T_{\mathrm{c}}$ two important qualitative changes in the spectra occur. First, due to the symmetry breaking the selection rules change (see Methods), such that the modes of A_{g} symmetry can appear in ac polarization geometry. For the ac spectra below 22 meV (where the Fano model fit is made), four additional modes appear - corresponding to $\mathrm{A}_g^{(1)}$-$\mathrm{A}_g^{(4)}$ modes. We perform three steps to account for these additional features: First, we use the phononic lineshape Eq. (7) to fit the corresponding features in aa polarization geometry to obtain the frequencies and HWHM for each of the $\mathrm{A}_g^{(1)}$-$\mathrm{A}_g^{(4)}$ modes [Fig. 7 (a-d)]. Second, we use Eq. (7) (see also Eq. (1) in [3]) to individually fit the three "leakage" modes in ac polarization geometry, with the frequencies and HWHM fixed; namely, the only free parameter is the light-scattering vertex. The vertex

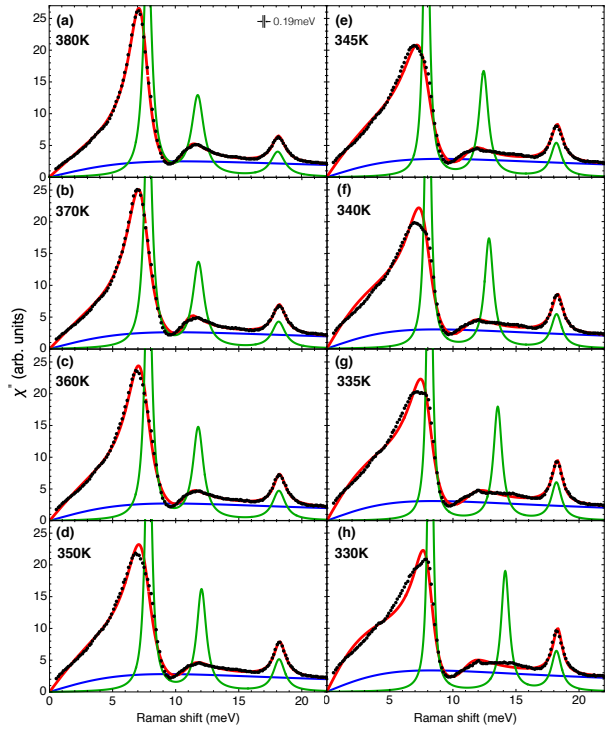

Supplementary Figure 3: Temperature dependence of Raman response χ'' in the ac scattering geometry for Ta_2NiSe_5 [3]. The data is shown by black dots, along with the Fano fits [Eq. (10)] shown as red curves. The spectral resolution is 0.19 meV. The bare optical phonon mode response is shown by green curves, and the bare excitonic continuum is shown by blue curves [see Eq. (14)].

values obtained are shown in Fig. 7 (e-h). Third, we subtract the associated response from the total one and then fit the remaining response with the model discussed below.

Additionally, not too far away from T_c, we have found that an additional enhancement of the low-energy response. We relate this observation with a quasiperiodic domain structure formed below T_c. In Fig. 4 we present transmission electron microscopy images of the sample. Thin domains along the a axis are resolved below T_c, but not above T_c. The average spacing $\bar{d}$ between these stripes along c-axis direction is on the order of 200 $\mathring{A}$. Acoustic phonon, scattering on this quasiperiodic structure, can take a recoil momentum of the order $2\pi/\bar{d}$; this way a finite $q_d = \pm 2\pi/\bar{d}$ phonon can contribute to the Raman intensity (where the momentum transfer is approximately zero). At finite q, introducing the acoustic phonon coordinate $x_q = \sqrt{q}u_q$, where u_q - is the Fourier transform of the atomic displacement amplitude, one obtains that the Green's function of the acoustic mode:

$$G_s(\omega, q) = -\left(\frac{1}{\omega - c_s q + i r_s q} - \frac{1}{\omega + c_s q + i r_s q}\right). \tag{15}$$

Its light-scattering vertex $t_{\rm s}(q)$ and coupling to the excitonic continuum $v_{\rm s}(q)$ are both proportional to the square root of wavevector: $t_{\rm s} = \tau_{\rm s}\sqrt{q}$ and $v_{\rm s} = \beta_{\rm s}\sqrt{q}$. The frequency $\omega_{\rm s}$ and the HWHM $\gamma_{\rm s}$ are both proportional to the wavevector: $\omega_{\rm s} = c_{\rm s}q$ and $\gamma_{\rm s} = r_{\rm s}q$, where $c_{\rm s}$ is the sound velocity, that can be deduced from the X-ray measurements [12] to be $c_{\rm s} \approx 30\,$meV Å away from $T_{\rm c}$. After introducing this mode, Eqs. (12-13) extend to

$$G_0' = \begin{pmatrix} G_{p1}^0 & 0 & 0 & 0 & 0 \\ 0 & G_{p2}^0 & 0 & 0 & 0 \\ 0 & 0 & G_{p3}^0 & 0 & 0 \\ 0 & 0 & 0 & G_s & 0 \\ 0 & 0 & 0 & 0 & G_e \end{pmatrix}, \tag{16}$$

$$V' = \begin{pmatrix} 0 & 0 & 0 & 0 & v_1 \\ 0 & 0 & 0 & 0 & v_2 \\ 0 & 0 & 0 & 0 & v_3 \\ 0 & 0 & 0 & 0 & \beta_{\rm s}\sqrt{q} \\ v_1 & v_2 & v_3 & \beta_{\rm s}\sqrt{q} & 0 \end{pmatrix}, \tag{17}$$

and the vertex for light-scattering process becomes $T' = \left(t_{p1}, t_{p2}, t_{p3}, \tau_{\rm s}\sqrt{q}, t_e\right)$.

Then the total response function containing coupling to acoustic mode for domain walls i lattice constants apart is given by

$$\chi_i'' \sim {\rm Im} T'^T G' T' \,. \tag{18}$$

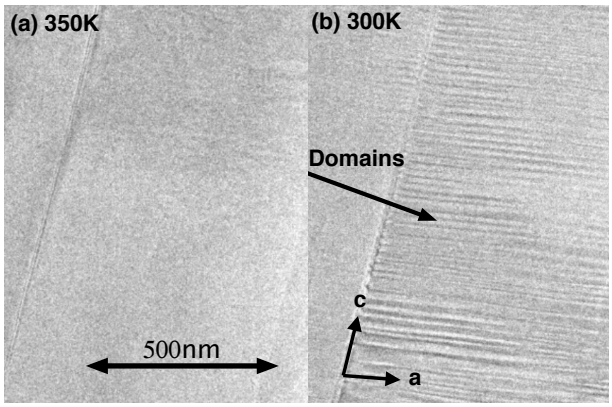

Supplementary Figure 4: Transmission electron microscopy images of the sample [3]: (a) at 350 K and (b) at 300 K. Structural domains with average spacing on the order of sizes of 200 $\mathring{A}$ can be directly observed for temperature below $T_{\rm c}$.

However, as has been noted above, the domain size is not the same for all domains; to take this into account we will assume that the spacing between stripes i in units of the crystal unit

cell constant c follows the Poisson distribution

$$P(i;\mu = \frac{\bar{d}}{c}) = \frac{\mu^i e^{-\mu}}{i!}, \tag{19}$$

where μ is average inter-domain distance in the number of c-direction unit cells. Recognizing that the low-frequency feature is inhomogeneously broadened by random distribution of the stripe distances, for the fitting procedure to the measured response function we perform summation over the distribution function:

$$\chi''(\omega) = \sum_{i=1}^{\infty} P(i;\mu)\chi_i''(\omega), \tag{20}$$

in which each $\chi_i''(\omega)$ is the full response function containing coupling to acoustic mode for domain walls i lattice constants apart. For fitting, we have taken $\beta = 7.7\,\text{meV}\,\text{Å}^{\frac{1}{2}}$ from the assumption that the static susceptibility including coupling to both acoustic and optical phonons should diverge at T_c (see Section S 1.3.4).

Supplementary Note 1.3.3 Fano fit parameters

The fits to the data, as well as the phononic and excitonic components, are shown in Fig. 3 of the main text. For the 300 K and 265 K spectra below T_c we also include the acoustic contribution due to coupling via quasi-periodic structure of domain walls. The value τ_s is 6.0 meV Å$^{\frac{1}{2}}$ at 300 K and 2.2 meV Å$^{\frac{1}{2}}$ at 265 K; the value r_s is 45 meV Å at both 300 K and 265 K.

The temperature dependence of the coupling strengths v_i, the light-scattering vertex t_e of the excitonic continuum, and the parameter Ω_e of the continuum is shown in Fig. 5. The frequency, linewidth, and light-scattering vertex of the three $B_{2\text{g}}$ phonon modes as a function of temperature are given in Fig. 6. In Fig. 5 (a), one observes that the continuum-phonon coupling strengths $v_{1,2}$ are almost constant above T_c and decrease in magnitude at lower temperatures. The third phonon is almost decoupled from the continuum at all temperatures, and essentially have a symmetric lineshape (see Fig. 3 of the main text). The signs of $v_{1,2}$ reflect the different shapes of the resulting asymmetric features: the $B_{2\text{g}}^{(1)}$ phonon peak is skewed to the left, while $B_{2\text{g}}^{(2)}$ is skewed in the opposite direction (see Fig. 2d and Fig. 3 of the main text). In Fig. 5 (b), one can see that the light-scattering vertex of the excitonic continuum is temperature independent. The parameter Ω_e has the same temperature dependence as the inverse bare static excitonic susceptibility (see Fig. 4 of the main text).

In Fig. 6 (a) - (c) we show the frequency ω_p and HWHM γ_p of the three $B_{2\text{g}}$ phonon modes. The frequencies increase on cooling, with the lower-energy $B_{2\text{g}}^{(1,2)}$ modes showing a pronounced increase around T_c. In the same region, all the three modes show a pronounced decrease of HWHM on cooling, suggesting an enhanced phonon scattering above T_c. Below 300 K, the temperature dependence of both frequency and HWHM of the phonon modes is in accordance with a simple model assuming anharmonic decay into two phonons with identical frequencies and opposite momenta [13]:

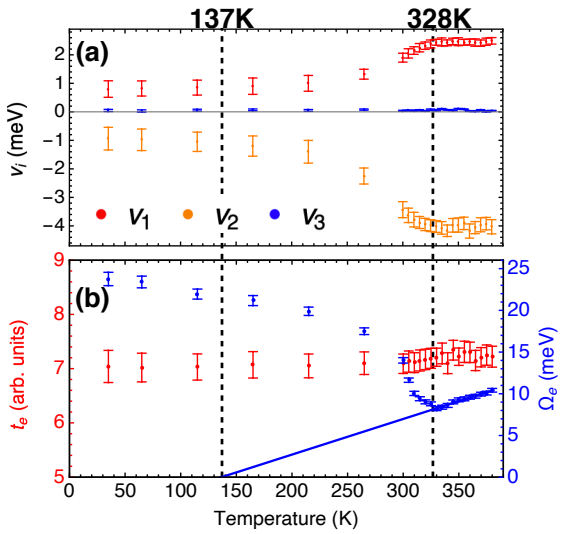

Supplementary Figure 5: Temperature dependence of (a) the coupling strengths $v_{1,2,3}$ of the three B_{2g} optical phonons to the excitonic continuum, and (b) the light-scattering vertex t_e and the parameter Ω_e of the excitonic continuum [3]. These values are obtained from the Fano lineshape fit, Eqs. (10-13,20).

$$\omega(T) = \omega_0 - \omega_2[1 + \frac{2}{e^{\hbar\omega_0/2k_BT} - 1}], \tag{21}$$

and

$$\gamma(T) = \gamma_0 + \gamma_2[1 + \frac{2}{e^{\hbar\omega_0/2k_BT} - 1}]. \tag{22}$$

The light-scattering vertex (t_p) as a function temperature is presented in Fig. 6 (d)-(f). Below T_c, the vertex values increase on cooling, most significantly for the $B_{2g}^{(3)}$ mode, reflecting the changes in the structure of these modes and the corresponding atomic displacement patterns below T_c.

In Fig. 7 we present the parameters used to subtract the additional $A_g^{(1)}$-$A_g^{(4)}$ modes appearing in the ac spectra at $T < T_c$. The temperature dependence of the frequency and HWHM is consistent with the anharmonic decay model; the vertex values become non-zero below the transition temperature, and tend to saturate at very low temperature.

Supplementary Note 1.3.4 Static susceptibility

The function (10,11) used to fit the finite-energy Raman response (by taking the imaginary part) can be also used to calculate the static B_{2g} susceptibility by simply taking its zero-frequency limit:

$$\chi_{ac}(0,T) = \sum_{ij} T_i G_{ij}(0) T_j. \tag{23}$$

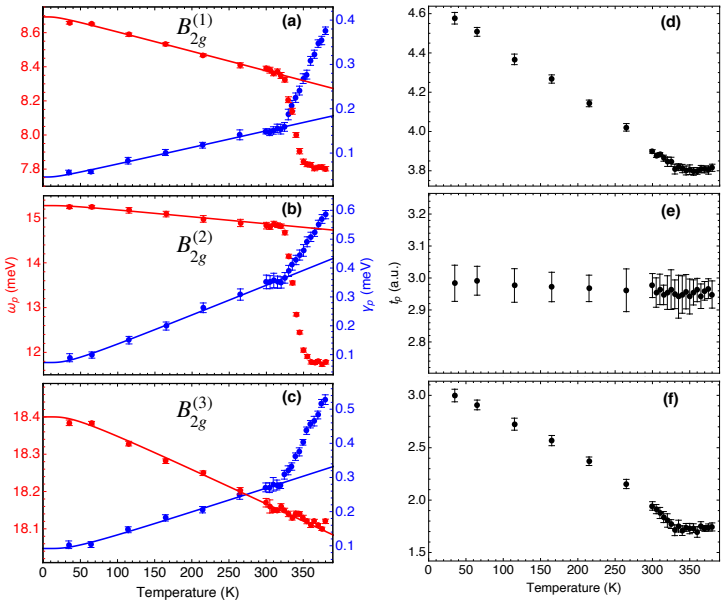

Supplementary Figure 6: Temperature dependence of (a)-(c) bare frequencies ($\omega_{\rm p}$) and HWHM ($\gamma_{\rm p}$), and (d)-(f) light-scattering vertex ($t_{\rm p}$) of the three B_{2g} optical phonons obtained from the Fano lineshape fit Eq. (10) [3].

This expression is used to calculate the combined susceptibility data for Fig. 5 in the main text. Additionally, one can define the purely electronic (continuum) and purely phononic parts of the susceptibility as:

$$\begin{aligned}\chi_{\rm cont}(0,T) &= \frac{t_{\rm e}^2(T)}{\Omega_{\rm e}(T)},\\ \chi_{\rm opt}(0,T) &= \sum_{i=1}^{3}\frac{t_{{\rm p}i}^2(T)}{2\omega_{{\rm p}i}(T)}.\end{aligned} \tag{24}$$

The critical temperature due to excitons and optical phonons $T_{\rm c}^{comb}$ (excluding the coupling to strain modes) can be obtained from Eq. (23); the condition for $\chi_{\rm ac}(0,T)$ to diverge is independent of the light-scattering vertex T_i, and is given by $\det G_{ij}^{-1}(0)=0$ resulting in the following equation:

$$\Omega_{\rm e}(T_{\rm c}^{comb}) - \sum_{i=1}^{3}\frac{2v_i^2}{\omega_{{\rm p}i}} = 0. \tag{25}$$

Using the values of v_i and $\omega_{{\rm p}i}$ above 350 K where they do not depend strongly on temperature and a linear extrapolation of $\Omega_{\rm e}(T)$ (Fig. 5) one obtains $T_{\rm c}^{comb}\approx 227$ K, consistent with Fig. 5b, where a linear extrapolation for $\omega_{{\rm p}i}$ (Fig. 4b of the main text, dashed lines) has been additionally used.

One can also include the contribution of acoustic phonons at $\mathbf{q}\to 0$ to get the full suscepti-

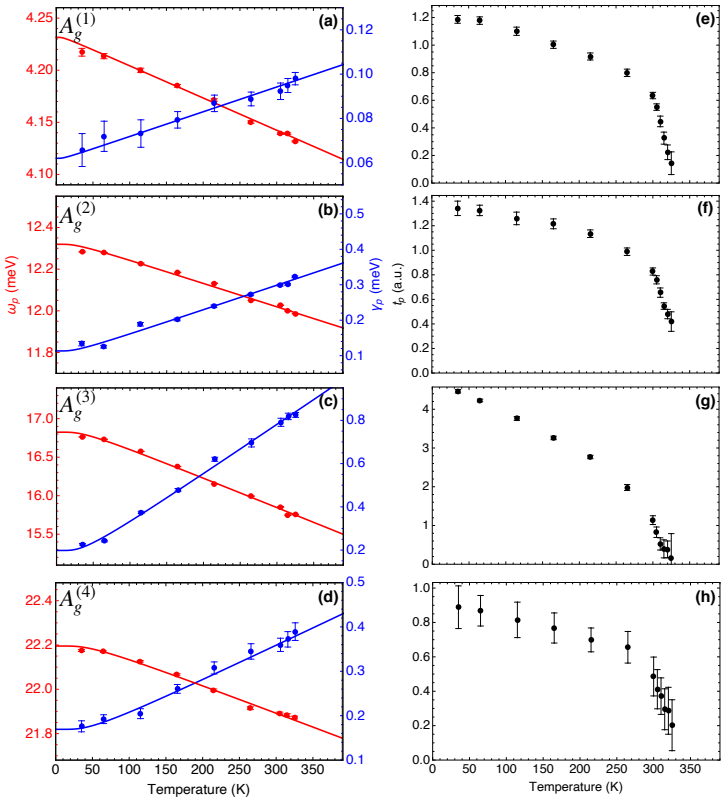

Supplementary Figure 7: Temperature dependence of (a)-(d) bare frequencies ($\omega_{\rm p}$) and HWHM ($\gamma_{\rm p}$), and (e)-(h) light-scattering vertex ($t_{\rm p}$) of the four $A_{\rm g}$ optical phonons obtained from the phononic lineshape fit Eq. (7) [3].

bility. Performing the same calculations as above, but using Eq. 16 for the Green's function and 17 for the coupling matrix with infinitesimal q one gets:

$$\Omega_{\rm e}(T_{\rm c}) - \sum_{i=1}^{3} \frac{2v_i^2}{\omega_{{\rm p}i}} - \frac{2\beta_{\rm s}^2}{c_{\rm s}} = 0. \tag{26}$$

One observes that the effect of the acoustic mode on $T_{\rm c}$ does not vanish in the $q \to 0$ limit despite the coupling is $\sim \sqrt{q}$. This equation allows to determine $\beta_{\rm s}$ used for fitting the domain-induced low-energy upturn below $T_{\rm c}$ discussed above.

The combined (excitonic interacting with phononic, red symbols in Fig. 5 of main text) static susceptibility could be also obtained by performing Kramers-Kronig transformation directly on the experimentally measured data. We have restricted the integration to 100 meV at high energy. A linear extrapolation of the data to zero intensity below 0.4 meV cutoff was used. In Table 1 we compare the static susceptibility calculated from the analytical Fano model to that obtained by Kramers-Kronig numerical transformation directly from the data. We note that the values obtained by numerical integration are systematically smaller than the values obtained from the

Table 1: The combined static B_{2g} susceptibility at three temperatures, calculated by two methods: using the analytical expression from the Fano model with the fitting parameters or by numerical Kramers-Kronig transformation.

Temperature (K)	380	330	310
$\chi_{ac}(0,T)$(a.u.) [Fano model]	15.0 (0.7)	19.6 (1.2)	18.4 (0.9)
$\chi_{ac}(0,T)$(a.u.) [Numerical KK]	14.1	18.5	17.4

analytical Fano model because of finite cutoff frequency (100 meV). The static susceptibility values derived by two methods are in good agreement.

Supplementary Note 1.3.5 Softening of the B_{2g} acoustic mode above T_c

Here we discuss the interpretation of the results of Nakano et al., [12] in light of our data. In particular, we show that the softening of the acoustic mode observed in those experiments can be actually attributed to the coupling of the acoustic mode to the softening excitonic continuum. The renormalized modes can be obtained by solving the equation $\det\{G(\omega)^{-1}-V\}=0$. As the relevant frequencies for the acoustic mode are much lower than that of the optical or excitonic modes, we can keep ω only in the bare acoustic mode's Green's function resulting in:

$$\omega^2 = \omega_s^2 - \frac{2v_s^2\omega_s}{\tilde{\Omega}_e(T)}, \tag{27}$$

where

$$\tilde{\Omega}_e(T) = \Omega_e(T) - \sum_{i=1}^{3}\frac{2v_i^2}{\omega_i}. \tag{28}$$

Note that at T_c the total static susceptibility must diverge, resulting in a condition $\det\{G(\omega, T=T_c)^{-1}-V\}=0$. This gives a constraint on the value of v_s: $\Omega_e(T_c)-\sum_{i=1}^{3}\frac{2v_i^2}{\omega_i}=\frac{2v_s^2}{\omega_s}$. Applying this result to the equation above we get

$$\omega^2 = \omega_s^2\left(1-\frac{\tilde{\Omega}_e(T_c)}{\tilde{\Omega}_e(T)}\right). \tag{29}$$

Finally, substituting $\omega_s = c_s^0 q$ one finds that the dispersion of the acoustic mode is given by $\omega=\tilde{c}_s q$, where

$$\tilde{c}_s(T) = c_s^0\sqrt{1-\frac{\tilde{\Omega}_e(T_c)}{\tilde{\Omega}_e(T)}}. \tag{30}$$

Note that from the above it follows that at T_c the sound velocity softens to zero, as is seen experimentally [12], even in the absence of an intrinsic lattice instability, i.e. purely due to exciton-phonon coupling.

One can also estimate the expected renormalization of the sound velocity away from T_c. Using the parameters extracted from the fits, we obtain $\tilde{c}_s(T = 400K)/c_s^0 \approx 0.65$. Experimentally, taking c_s^0 to be the low-temperature value of c_s (which also agrees with DFT calculations) [12] one obtains $\tilde{c}_s(T = 400K)/c_s^0 \approx 0.65$, in excellent agreement with the estimate from Eq. (30). Thus, our observations suggest that Ta_2NiSe_5 does not have a ferroelastic instability, and that the softening of the acoustic modes can be well described as being due to the coupling to the softening excitonic continuum instead.

Supplementary Note 1.4 Additional details for low-energy Raman spectra

In Fig. 2f of the main text we present the temperature dependence of the low-energy Raman response in ac geometry. In Fig. 8 we present the comparison of the low-energy Raman response in aa and ac geometries. One notes the absence of the strong Fano features in aa geometry, comparable to those in ac geometry (see also Fig. 2f of the main text) at all temperatures. We also note that the A_g phonon modes exhibit no softening upon cooling towards the transition temperature; instead, their frequencies follow the anharmonic model between 360 and 35 K [3]. Additionally, the appearance of "leakage" between aa and ac geometries is clearly visible below T_c (Fig. 8 d-h).

Supplementary Note 1.5 Additional details for high-energy Raman spectra

Supplementary Note 1.5.1 Details of the temperature dependence of the high-energy ac spectra

In Fig. 2e of the main text we compare the high-energy Raman response in aa and ac scattering geometries on the same scale. In Fig. 9b below we show the enlarged ac spectra where the stark contrast to the aa (Fig. 9a) response can be better appreciated: there is no pronounced redistribution of intensity and no gap opening on cooling. The intensity actually increases on cooling below 200 meV, which can be partially attributed to "leakage" from aa geometry below T_c -see subSec. Supplementary Note 1.5.3 below.

Supplementary Note 1.5.2 Intensity redistribution in high-energy Raman spectra

Here we illustrate the evolution of intensity in aa and ac geometries on cooling by computing the integral $I_{aa(ac)}(\omega^*) = \int_0^{\omega*} \frac{\chi''_{aa(ac)}(\omega)}{\omega} d\omega$ (Fig. 10). For $\omega^* \to \infty$ this quantity is proportional to the static susceptibility in the respective geometry, while the $\omega*$ dependence allows to understand the contribution of different frequency ranges.

For aa polarization (Fig. 10a), one observes that at frequencies larger than 50 meV, the spectral weight gets suppressed on cooling below around 300 meV, but then recovers at 500

meV to an almost temperature-independent value. This is consistent with the absence of strong temperature dependence of the static A_g susceptibility that has no instability in Ta_2NiSe_5. Moreover, this shows that unlike in a mean-field theory (see section S2 below) where the A_g signal should vanish in the absence of the order parameter, the integral at 500 meV is roughly constant across T_c, consistent with the presence of signatures of the excitonic pairing (the pseudogap) well above T_c observed in ARPES [14].

In ac geometry, on the other hand, $I_{ac}(500\text{meV})$ is strongly dependent on temperature. However, $I_{ac}(\omega^*)$ appear to be almost parallel above around 30 meV, without any signs of redistribution as in aa geometry. This suggests that the temperature dependence arises due to the contribution of the lower energies to the integral. Indeed, there is a strong enhancement at the lowest frequencies on cooling from 380 K to 310 K explained by the softening of the excitonic continuum (see Fig. 3 of the main text and Fig. 3), and a suppression on further

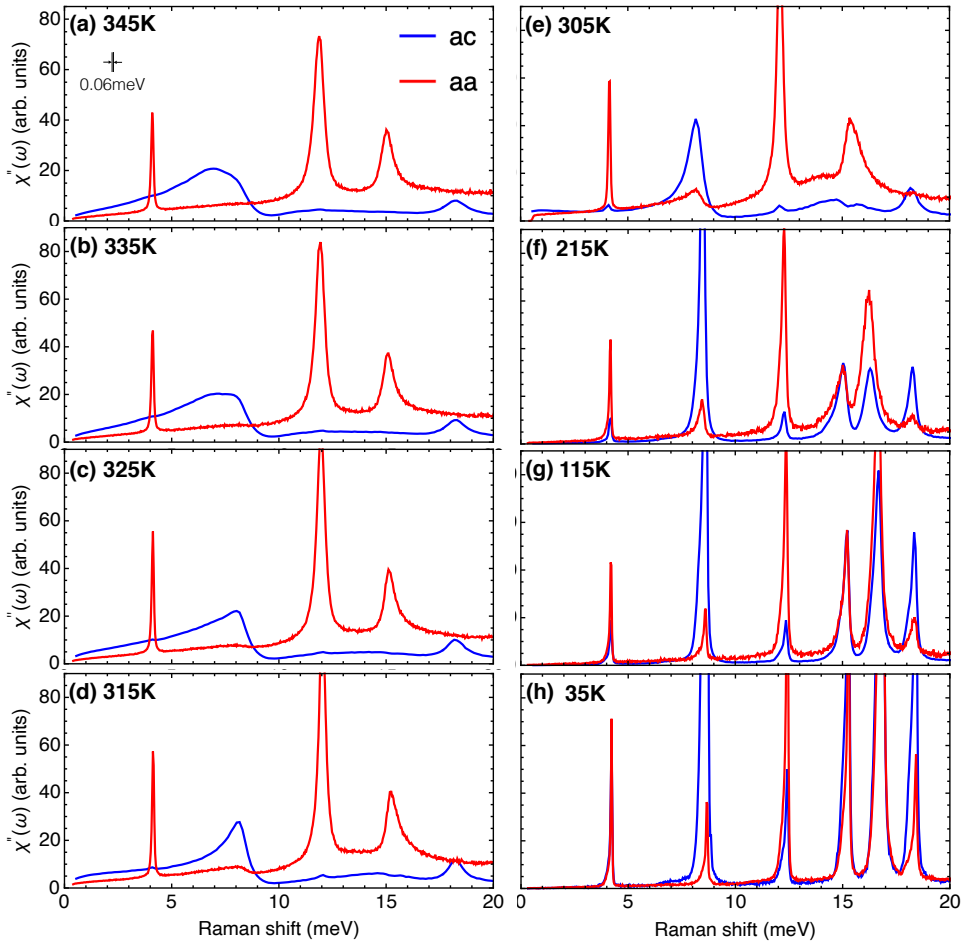

Supplementary Figure 8: Comparison of the temperature dependencies of the low-frequency Raman response in aa and ac scttering geometries at temperatures between 345 and 35 K.

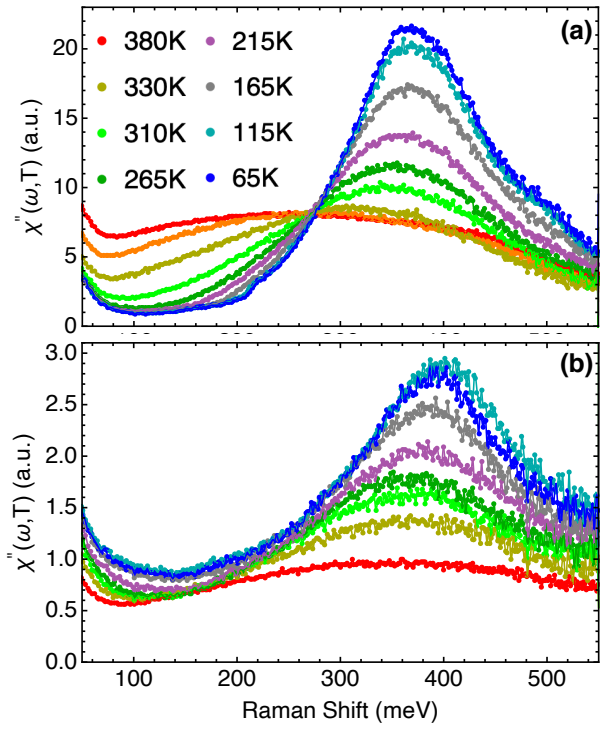

Supplementary Figure 9: Temperature dependence of the high-energy Raman response in (a) aa and (b) ac geometries.

cooling. The enhancement on cooling from 265 K to 35 K can be seen to arise from energies around $15-20$ meV where a contribution of phonon "leakage" (which grows on cooling) from aa geometry is prominent.

Overall, we have shown that the pronounced redistribution of the high-energy Raman response is characteristic of aa geometry, but not ac geometry, demonstrating that the emergence of the strong peak in the ordered phases, shown in Fig. 2e of the main text, is indeed specific for aa geometry.

Supplementary Note 1.5.3 "Leakage" in high-energy Raman spectra at low temperatures

Here we demonstrate that a large part of the ac Raman intensity (Fig. 2e) can be attributed to the change in the Raman selection rules below T_c. In analogy to the phonons, one may expect the intensity from aa geometry to "leak" into ac geometry and vice versa. As aa intensity is significantly larger in the high-energy region than the ac one, we can neglect the leakage of ac into aa, and consider only the former effect. Consequently, we have analyzed $\chi''_{\rm ac}(\omega) - p\cdot\chi''_{\rm aa}(\omega)$, where $0 < p < 1$. Intriguingly, for $p = 0.07$ (Fig. 11), we observe the resulting intensity (shown in purple) to be featureless below around 310 meV, while for other values of p a residual energy

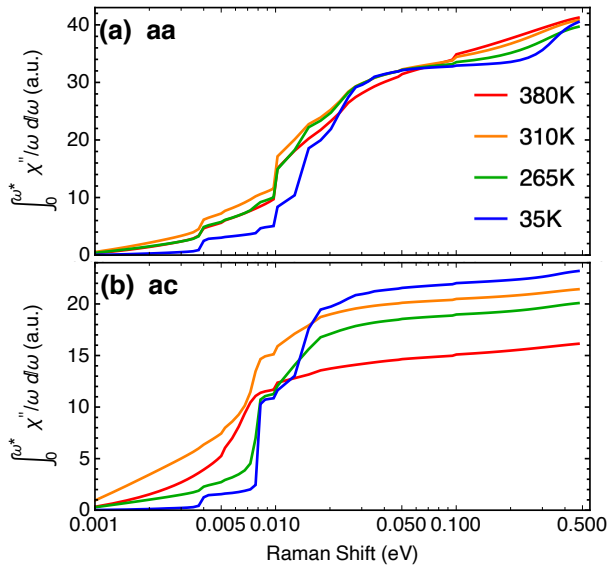

Supplementary Figure 10: The integral $\int_0^{\omega*} \frac{\chi''_{aa(ac)}(\omega)}{\omega} d\omega$ as a function of the Raman shift $\omega*$ for aa (**a**) and ac (**b**) polarization geometries.

dependence in this region is observed. This coincidence of lineshapes up to a background

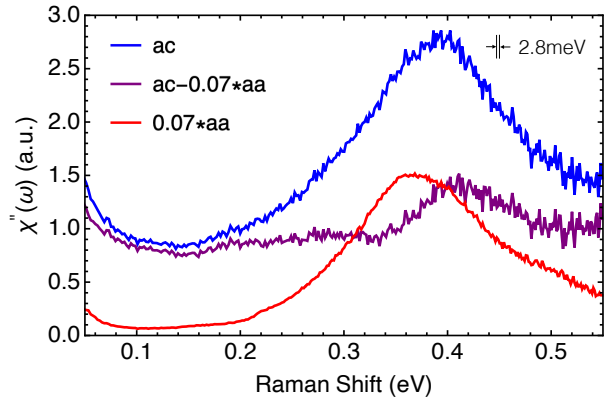

Supplementary Figure 11: "Leakage" analysis of the high-energy Raman data at 35 K. Blue line is the measured ac-polarization data; subtracting 7% of the aa-polarization data (red line) from the ac-polarization data one obtains an almost flat intensity below about 0.33 eV (purple line), suggesting that there is a 7% leakage between aa and ac-polarized data at high-energies. The spectral resolution is 2.8 meV.

constant below around 310 meV suggests that the "intrinsic" ac intensity, corresponding to the interband transitions, is actually represented by the purple curve, Fig. 11. It follows then that not only the intensity in ac geometry is much weaker, but also that its lineshape is different,

characterized by the appearance of intensity at higher energies than in aa geometry. The latter observation is consistent with the prediction of the mean-field model, where the intensity in aa geometry is expected to be peaked at the gap edge, while the one in ac geometry only starts to grow at the gap edge and should be maximal at higher energies.

Supplementary Note 2 Raman scattering in an excitonic insulator at low temperatures

We consider a model with an electron-like conduction band and hole-like valence band described by the hamiltonian

$$\hat{H}_0 = \sum_{\mathbf{p},\sigma} \varepsilon_{\mathrm{c}}(\mathbf{p}) \hat{c}^{\dagger}_{c,\sigma}(\mathbf{p}) \hat{c}_{c,\sigma}(\mathbf{p}) + \varepsilon_{\mathrm{v}}(\mathbf{p}) \hat{c}^{\dagger}_{v,\sigma}(\mathbf{p}) \hat{c}_{v,\sigma}(\mathbf{p}), \tag{31}$$

where the band operators at the Γ point transform under irreducible representations I_1 and I_2 of the point group above T_{c} - $D_{2\mathrm{h}}$, such that $I_1 \otimes I_2 \equiv B_{2\mathrm{g}}$. The latter requires the hybridization between the two bands at the Γ point to vanish; however, below T_{c} the point-group symmetry is reduced to $C_{2\mathrm{h}}$ such that $B_{2\mathrm{g}}$ merges with the trivial A_{g} representation into a single one, allowing for the $c-v$ hybridization at the Γ point. Thus, the quantity of the form $\langle \hat{c}^{\dagger}_{c,\sigma} \hat{c}_{v,\sigma'} \rangle$ may serve as the order parameter for the phase transition from $D_{2\mathrm{h}}$ to $C_{2\mathrm{h}}$. One needs to be make sure though, that the average doesn't break any additional symmetries. In particular, no spin anisotropy or magnetism have been observed in Ta_2NiSe_5, requiring $\langle \hat{c}^{\dagger}_{c,\sigma} \hat{c}_{v,\sigma'} \rangle = W \delta_{\sigma,\sigma'}$. Moreover, time-reversal symmetry that acts as a complex conjugation, if spin is ignored, requires W to be real. This suggests that in contrast to true bosonic condensates, there is no $U(1)$ degeneracy of the order parameter in an excitonic insulator, that is instead reduced to Z_2. The general reason for that is that while there is a global $U(1)$ symmetry due to particle number conservation, the number of c and v electrons are not separately conserved (which would yield a $U(1) \times U(1)$ symmetry otherwise), suggesting that the exciton number is not a conserved quantity, i.e. $U(1) \times U(1)$ is initially broken to $U(1) \times Z_2$ already in the $D_{2\mathrm{h}}$ phase. The mechanism of this breaking may be either due to pair-hopping interaction between bands, or coupling to phonons.

While most of the equations below are generic, we will use the following form of the dispersion to illustrate the results:

$$\varepsilon_{\mathrm{c}}(\mathbf{p}) \approx \frac{p_x^2 \pm p_0^2}{2m_{\mathrm{c}}};\ \varepsilon_{\mathrm{v}}(\mathbf{p}) \approx -\frac{p_x^2 \pm p_0^2}{2m_{\mathrm{v}}}, \tag{32}$$

where with the $+$ sign dispersion is semiconducting, while it is semimetallic for $-$ sign; here p_0 is equal for both bands due to the charge compensation condition. While the dispersion (32) is strictly one-dimensional, we assume that the transition itself would have three-dimensional character either due to terms neglected in (32) (corresponding to interchain hopping along b and c directions $t_{b,c}$), or due to the coupling to optical phonons or acoustic strain fields, that are

expected to have a three-dimensional dispersion. Due to the layered structure of Ta_2NiSe_5 one may also expect that the three-dimensional character would be rather weak, with an extended 2D-like regime. However, due to discrete nature of the broken Z_2 symmetry, this is not expected to significantly reduce T_c as even in strictly two dimensions the transition is allowed to occur.

We introduce a 2×2 "band space" and rewrite $\hat{H}_0$ using Pauli matrices τ_i and spinors $\Psi_{\mathbf{p},\sigma} = (\hat{c}_{c,\sigma}(\mathbf{p}), \hat{c}_{v,\sigma}(\mathbf{p}))$:

$$\hat{H}_0 = \sum_{\mathbf{p},\sigma} \Psi^\dagger_{\mathbf{p},\sigma}(E(\mathbf{p}) + \xi(\mathbf{p})\tau_3)\Psi_{\mathbf{p},\sigma};\ E(\mathbf{p}) = \frac{\varepsilon_c(\mathbf{p}) + \varepsilon_v(\mathbf{p})}{2};\ \xi(\mathbf{p}) = \frac{\varepsilon_c(\mathbf{p}) - \varepsilon_v(\mathbf{p})}{2}. \quad (33)$$

In what follows we will omit $(\mathbf{p})$ in $\xi(\mathbf{p}), E(\mathbf{p})$, where that doesn't lead to a confusion. At low temperatures, the mean field Hamiltonian including the excitonic order parameter W is

$$\hat{H}_{MF} = \begin{bmatrix} \hat{c}_c(\mathbf{p}) \\ \hat{c}_v(\mathbf{p}) \end{bmatrix}^\dagger \begin{bmatrix} \varepsilon_c(\mathbf{p}) & W \\ W & \varepsilon_v(\mathbf{p}) \end{bmatrix} \begin{bmatrix} \hat{c}_c(\mathbf{p}) \\ \hat{c}_v(\mathbf{p}) \end{bmatrix}. \quad (34)$$

Note that, unlike in a superconductor [15], the mean-field hamiltonian (34) explicitly conserves the total particle number $N = \sum_{\mathbf{p}} \hat{c}^\dagger_p \hat{c}_p + \hat{v}^\dagger_p \hat{v}_p$ and consequently vertex corrections for Raman scattering are not required to ensure it. Diagonalizing Eq. (34) , one obtains the following eigenvalues and eigenvectors:

$$\begin{gathered} \varepsilon_\pm(\mathbf{p}) = E(\mathbf{p}) \pm \sqrt{\xi^2(\mathbf{p}) + W^2}; \\ \Psi_\pm(\mathbf{p}) = [u_\pm(\mathbf{p}), v_\pm(\mathbf{p})]^T, \\ u_\pm(\mathbf{p}) = \pm\sqrt{\frac{1}{2}\left(1 \pm \frac{\xi}{\sqrt{\xi^2 + W^2}}\right)};\ v_\pm(\mathbf{p}) = \sqrt{\frac{1}{2}\left(1 \mp \frac{\xi}{\sqrt{\xi^2 + W^2}}\right)}. \end{gathered} \quad (35)$$

The factors $u_\pm, v_\pm$ are analogous to the BCS coherence factors in a superconductor.

We consider the Raman scattering in the non-resonant approximation, where the effective coupling of the electrons to the two-photon process is described by $\sum_{\mathbf{q}} \hat{R}^{ij}\mathbf{A}_i(\mathbf{q})\mathbf{A}_j(-\mathbf{q})$, where $\hat{R}^{ij} = \sum_{\mathbf{p}} \gamma^{ij}_{\alpha\beta} c^\dagger_\alpha(\mathbf{p}) c_\beta(\mathbf{p})$ is the Raman vertex [16], where we additionally neglect the momentum dependence of $\gamma^{ij}_{\alpha\beta}$. The Raman susceptibility in the polarization geometry set by i and j is determined by the transition rate of the electronic system due to the perturbation by $\hat{R}^{ij}$. The symmetry restricts the possible form of $\hat{R}^{ij}$ [16]; for our case $\hat{R}^{aa}$ has to be of A_g symmetry and $\hat{R}^{ac}$ - B_{2g} symmetry. Taking these constraints into account the Raman vertices take the form

$$\hat{R}_{aa} = \sum_p g_c \hat{c}^\dagger_p \hat{c}_p + g_v \hat{v}^\dagger_p \hat{v}_p;\ \hat{R}_{ac} = g_{ac} \sum_p \hat{c}^\dagger_p \hat{v}_p + \hat{v}^\dagger_p \hat{c}_p, \quad (36)$$

where $\hat{R}_{aa}$ corresponds to aa polarization geometry and $\hat{R}_{ac}$ - to ac geometry. Using Fermi's Golden rule we evaluate the probability to find:

$$2\pi \int |\langle +|\hat{R}|-\rangle|^2 \delta(\varepsilon_+(\mathbf{p}) - \varepsilon_-(\mathbf{p}) - \omega) \frac{2d\mathbf{p}}{(2\pi)^D},$$

where we assumed that the system is fully gapped, i.e. $\varepsilon_+(\mathbf{p}) > 0 > \varepsilon_-(\mathbf{p})$ for all values of $\mathbf{p}$. Note that under this assumption the resulting expression does not depend on $E(\mathbf{p})$.

Supplementary Note 2.1 Semimetallic case

In this case the bands are assumed to cross in the normal state, similar to the Fig. 1d of the main text. In this case, one can linearize the dispersion near the band crossing $\xi(\mathbf{p}) = 0$, such that $\frac{2d\mathbf{p}}{(2\pi)^D} \approx \nu_0 d\xi$, ν_0 being the density of states. Using the definition of the Raman vertex (36) and the eigenvectors obtained in (35) one gets

$$I_{R_{\rm ac}} \sim \frac{4\pi g_{\rm ac}^2 \nu_0 \sqrt{\omega^2/4 - W^2}}{\omega}\theta(\omega - 2W);\ I_{R_{\rm aa}} \sim \frac{\pi(g_{\rm c} - g_{\rm v})^2 \nu_0 W^2}{\omega\sqrt{\omega^2/4 - W^2}}\theta(\omega - 2W), \tag{37}$$

where we used that $u_+v_- + u_-v_+ = \frac{\xi}{\sqrt{\xi^2+W^2}}$; $u_+u_- + v_+v_- = 0$; $u_+u_- - v_+v_- = -\frac{W}{\sqrt{\xi^2+W^2}}$ and $\delta(2\sqrt{\xi^2+W^2} - \omega) = \frac{\delta(\xi \pm \sqrt{\omega^2/4 - W^2})}{2\xi/\sqrt{\xi^2+W^2}}$. Note that in the absence of the order parameter ($W = 0$), the Hamiltonian (34) would respect the conservation of c and v particle numbers separately, leading to a zero Raman response in aa geometry, which couples to densities of c and v fermions. Also, one notices that the aa intensity vanishes when $g_{\rm c} = g_{\rm v}$, i.e. when the Raman vertex (36) becomes just the total density operator. This further shows that particle number conservation is respected in our calculation.

Supplementary Note 2.2 Semiconducting case

In this case there is a direct gap between the two bands without hybridization. We use the 1D dispersion relation 32 with the "+" sign, such that the direct gap is $2E_0 \equiv \frac{p_0^2}{\mu}$, where $\mu = 2m_{\rm c}m_{\rm v}/(m_{\rm c} + m_{\rm v})$ is the effective mass. For the Raman intensity one gets then

$$I_{R_{\rm ac}} \sim 2g_{\rm ac}^2 \int \frac{(p^2/(2\mu) + E_0)^2}{(p^2/(2\mu) + E_0)^2 + W^2}\delta(2\sqrt{(p^2/(2\mu) + E_0)^2/4 + W^2} - \omega)dp,$$
$$I_{R_{\rm aa}} \sim \frac{(g_{\rm c} - g_{\rm v})^2}{2} \int \frac{W^2}{(p^2/(2\mu) + E_0)^2 + W^2}\delta(2\sqrt{(p^2/(2\mu) + E_0)^2 + W^2} - \omega)dp.$$

The result of the integration is:

$$I_{R_{\rm ac}} \sim 2g_{\rm ac}^2 \frac{\sqrt{2\mu}}{\omega\sqrt{\sqrt{\omega^2/4 - W^2} - E_0}}\theta(\omega - 2\sqrt{W^2 + E_0^2}),$$
$$I_{R_{\rm aa}} \sim \frac{(g_{\rm c} - g_{\rm v})^2}{2} \frac{\sqrt{2\mu}}{\omega\sqrt{\sqrt{\omega^2/4 - W^2} - E_0}} \frac{W^2}{\omega^2/4 - W^2}\theta(\omega - 2\sqrt{W^2 + E_0^2}). \tag{38}$$

Most important difference from the semimetallic case is that intensities in both geometries show singularities at the gap edge $\omega = 2\sqrt{W^2 + E_0^2}$. The intensity at the gap edge in aa geometry is additionally multiplied by a factor W^2/E_0^2. Thus, for the case $E_0 \ll W$ the intensity in the aa geometry is expected to dominate. However, for strongly semiconducting case $E_0 \gg W$, the singuarity in the aa geometry is expected to be greatly suppressed by W^2/E_0^2, at odds to the experimental observation in Fig. 2c of the main text. While the shapes of the singularities here are related to the 1D form of the dispersion taken, we expect the qualitative arguments on the intensity dependencies on the order parameter value to hold even when the effects of non-1D dispersion are taken into account, as those are expected mostly to smear the singularity at the band edge.

Overall, the absence of a discernible singularity in Fig. 2c in ac geometry strongly favors the semimetallic state.

Supplementary Note 2.3 Effects of a nonlocal order parameter

The non-locality of the order in real space results in the order parameter in momentum space being momentum-dependent, i.e. $W(\mathbf{p})$. Away from Γ point, time reversal and inversion symmetry combined require only that $W(\mathbf{p}) = W^*(-\mathbf{p})$, and thus $W(\mathbf{p})$ can be complex, generically written as $W(\mathbf{p}) = |W|(\mathbf{p})e^{i\phi(\mathbf{p})}$, where $\phi(\mathbf{p}) = -\phi(-\mathbf{p})$. Generalizing 35 with the momentum-dependent order parameter is straightforward and results in the new eigenvalues and eigenvectors:

$$\begin{gathered}\varepsilon_\pm(\mathbf{p}) = E(\mathbf{p}) \pm \sqrt{\xi^2(\mathbf{p}) + |W|^2(\mathbf{p})};\\ \Psi_\pm(\mathbf{p}) = [u_\pm(\mathbf{p}), v_\pm(\mathbf{p})]^T,\\ u_\pm(\mathbf{p}) = \pm\sqrt{\frac{1}{2}\left(1 \pm \frac{\xi}{\sqrt{\xi^2 + |W|^2(\mathbf{p})}}\right)};\ v_\pm(\mathbf{p}) = e^{-i\phi(\mathbf{p})}\sqrt{\frac{1}{2}\left(1 \mp \frac{\xi}{\sqrt{\xi^2 + |W|^2(\mathbf{p})}}\right)}.\end{gathered} \tag{39}$$

For the semiconducting case, assuming the $\mathbf{p}$ dependence of $|W|(\mathbf{p})$ does not shift the gap minimum from the Γ point $\phi(0) = 0$ and the results for the Raman intensities are the same as described above. For the semimetallic case, however, the result changes due to the presence of a nonzero phase. Assuming the gap to open at p_F and a quasi-one dimensional band structure (consistent with ARPES experiments [17; 18; 19]), we get close to the gap edge

$$\begin{gathered}I_{R_{\rm ac}} \sim 4\pi g_{\rm ac}^2 \nu_0 \left(\cos^2(\phi(p_F))\frac{\sqrt{\omega^2/4 - |W|^2(p_F)}}{\omega} + \frac{1}{2}\sin^2(\phi(p_F))\frac{\omega}{\sqrt{\omega^2/4 - |W|^2(p_F)}}\right)\theta(\omega - 2W);\\ I_{R_{\rm aa}} \sim \frac{\pi(g_{\rm c} - g_{\rm v})^2\nu_0|W|^2(p_F)}{\omega\sqrt{\omega^2/4 - |W|^2(p_F)}}\theta(\omega - 2|W|(p_F)).\end{gathered} \tag{40}$$

One observed that while $I_{R_{\rm aa}}$ has not changed, $I_{R_{\rm ac}}$ now contains a contribution, that diverges at the gap edge with its amplitude proportional to $\sin^2(\phi(p_F))$. This result is not expected to

affect the results qualitatively as p_F in Ta_2NiSe_5 is quite small and $\sin^2(\phi(p_F)) \sim k_F^2 a_0^2$, a_0 being the lattice constant: for $k_F \sim 0.1\,\text{Å}^{-1}$ [17] and $a_0 = 3.49$ Å[12], one gets the estimate $k_F^2 a_0^2$ of the order $0.12 \ll 1$. This estimate holds for, e.g. the recently proposed [20] case of $W(\mathbf{k}) = W_0 e^{ik_x a}$ (as is given in the Supplementary material to that paper). Additionally, this effect of non-locality can contribute to the apparent "leakage" of the aa intensity discussed in S1.3.

Supplementary Note 2.4 Corrections to the Raman vertex in the ordered state

Strictly speaking, at $T < T_c$ the irreps A_g and B_{2g} mix into a single A_g representation and thus the generic form of the Raman vertex operators may mix the ones at $T > T_c$. However, this mixing is apparently rather small in the system, as the ratio of intensities in cross polarization vs. the one in parallel polarizations is below $1/10$. A possible explanation for that is that in the effective mass approximation the appearance of the order parameter does not directly affect the mass.

Supplementary Note 2.5 Effects of disorder

Additionally, a remnant low-energy electronic continuum contribution is observed at low temperatures in Fig. 3g of the main text. Here we show that it can be attributed to the effect of disorder. In particular, we model disorder by a varying chemical potential $V(\mathbf{r})\tau_0$. If considered in Thomas-Fermi approximation to (34), is is seen that local $V > W$ creates a metallic "puddle"; due to the absence of translational invariance metals are expected to result in a Drude form of the Raman susceptibility at $q = 0$ due to particle-hole excitations [16], as is observed in the experiment.

Supplementary References

[1] Lu, Y. F. *et al.* Zero-gap semiconductor to excitonic insulator transition in Ta_2NiSe_5. *Nat. Commun.* **8**, 14408 (2017).

[2] Hayes, W. & Loudon, R. *Scattering of Light by Crystals* (Dover Publications, London, 2004).

[3] Ye, M. *et al.* Lattice dynamics of the $Ta_2Ni(Se_{1-x}S_x)_5$ excitonic insulator candidates. *Preprint at https://arxiv.org/abs/2102.07912 (2021)* .

[4] Fano, U. Effects of configuration interaction on intensities and phase shifts. *Phys. Rev.* **124**, 1866–1878 (1961).

[5] Klein, M. V. Electronic Raman scattering. In Cardona, M. (ed.) *Light Scattering in Solids I*, vol. 8, chap. 4, 147–202 (Springer-Verlag, Berlin, 1983).

[6] Blumberg, G., Klein, M. V., Börjesson, L., Liang, R. & Hardy, W. N. Investigation of the temperature dependence of electron and phonon raman scattering in single crystal yba2cu3o6.952. *Journal of Superconductivity* **7**, 445–448 (1994).

[7] Wu, S.-F. *et al.* Coupling of fully symmetric As phonon to magnetism in $\mathrm{Ba(Fe_{1-x}Au_x)_2As_2}$. *Phys. Rev. B* **102**, 014501 (2020).

[8] Goldenfeld, N. *Lectures on phase transitions and the renormalization group* (CRC Press, 2018).

[9] Yusupov, R. *et al.* Coherent dynamics of macroscopic electronic order through a symmetry breaking transition. *Nature Physics* **6**, 681–684 (2010).

[10] Zong, A. *et al.* Dynamical slowing-down in an ultrafast photoinduced phase transition. *Phys. Rev. Lett.* **123**, 097601 (2019).

[11] Schuller, I. K. & Gray, K. E. Time-dependent ginzburg–landau: From single particle to collective behavior. *Journal of Superconductivity and Novel Magnetism* **19**, 401–407 (2006).

[12] Nakano, A. *et al.* Antiferroelectric distortion with anomalous phonon softening in the excitonic insulator $\mathrm{Ta_2NiSe_5}$. *Phys. Rev. B* **98**, 045139 (2018).

[13] Klemens, P. G. Anharmonic Decay of Optical Phonons. *Phys. Rev.* **148**, 845–848 (1966).

[14] Seki, K. *et al.* Excitonic Bose-Einstein condensation in $\mathrm{Ta_2NiSe_5}$ above room temperature. *Phys. Rev. B* **90**, 155116 (2014).

[15] Klein, M. V. & Dierker, S. B. Theory of Raman scattering in superconductors. *Phys. Rev. B* **29**, 4976–4991 (1984).

[16] Devereaux, T. P. & Hackl, R. Inelastic light scattering from correlated electrons. *Rev. Mod. Phys.* **79**, 175–233 (2007).

[17] Okazaki, K. *et al.* Photo-induced semimetallic states realised in electron–hole coupled insulators. *Nat. Commun.* **9**, 4322 (2018).

[18] Fukutani, K. *et al.* Electrical tuning of the excitonic insulator ground state of $\mathrm{Ta_2NiSe_5}$. *Phys. Rev. Lett.* **123**, 206401 (2019).

[19] Chen, L. *et al.* Doping-controlled transition from excitonic insulator to semimetal in $\mathrm{Ta_2NiSe_5}$. *Phys. Rev. B* **102**, 161116 (2020).

[20] Mazza, G. *et al.* Nature of symmetry breaking at the excitonic insulator transition: $\mathrm{Ta_2NiSe_5}$. *Phys. Rev. Lett.* **124**, 197601 (2020).